Synthesis and acetone sensing properties of $ZnFe_2O_4$/rGO gas sensors

Kaidi Wu[1,2], Yifan Luo[1], Ying Li[1] and Chao Zhang[*1]

Address:
[1]College of Mechanical Engineering, Yangzhou University, Yangzhou 225127, P.R. China and [2]College of Hydraulic Science and Engineering, Yangzhou University, Yangzhou 225009, P.R. China

Email:
Chao Zhang[*] - zhangchao_cqu@hotmail.com

* Corresponding author

Abstract

Hollow spheres of pure $ZnFe_2O_4$ and of composites of $ZnFe_2O_4$ and reduced graphene oxide (rGO) with different rGO content were prepared via a simple solvothermal method followed by a high-temperature annealing process in an inert atmosphere. The X-ray diffraction analysis confirmed that the introduction of rGO had no effect on the spinel structure of $ZnFe_2O_4$. In addition, the results of field-emission scanning electron microscopy and (high-resolution) transmission electron microscopy indicated that the synthesized samples had the structure of hollow spheres distributed uniformly onto rGO nanosheets. The diameters of the spheres were determined as about 600–1000 nm. The gas sensing test revealed that the introduction of rGO improved the performance of the sensing of acetone to low concentration, and the $ZnFe_2O_4$/rGO composite gas sensor containing 0.5 wt % of rGO exhibited a high sensitivity in sensing test using 0.8–100 ppm acetone at 200 °C. The response of the 0.5 wt % $ZnFe_2O_4$/rGO sensor to 0.8 ppm acetone was 1.50, and its response to 10 ppm acetone was 8.18, which is around 2.6 times more pronounced than the response of pure $ZnFe_2O_4$ (10 ppm, 3.20). Moreover, the sensor showed a wide linear range and good selectivity.

Introduction

As a synthetic raw material in industrial production, acetone is chemically active and extremely flammable. It is toxic if its concentration exceeds 173 ppm, and long-term exposure to acetone poses a serious threat to human health [1,2]. Furthermore, acetone is also a fat metabolite in the human body. According to the related literature, the concentration of acetone in the exhaled gas of healthy people is less than 0.8 ppm, while that in exhaled gas of diabetic patients is higher than 1.8 ppm [3,4]. In this view, it may be possible to diagnose diabetes using a nondestructive testing technology based on sensing acetone. Thus, it is necessary to develop novel micro/nanomaterials, which can be applied as high-performance gas sensors to detect acetone at low concentration or to monitor variations of its concentration.

Due to their excellent properties and cost efficiency, gas sensors based on metal oxide semiconductors, such as ZnO [5], SnO_2 [6], WO_3 [7], TiO_2 [8], $Er-SnO_2$ [9], $Au-In_2O_3$ [10], $GO-WO_3$ [11] and $Ni-SnO_2/G$ [12] have been widely studied until now. However, their sensing properties regarding low amounts of acetone still need to be enhanced. As a dual metal oxide, AB_2O_4 spinel materials received much attention in the field of gas sensing [13,14]. With a unique spinel structure and a narrow bandgap width ($\approx$1.94 eV), zinc ferrite ($ZnFe_2O_4$) has remarkable properties and shows good potential in the field of gas sensing. It was reported that small, well-dispersed $ZnFe_2O_4$ nanoparticles showed a good selectivity to acetone at 200 °C, but the detection limit was only 5 ppm [15]. Porous $ZnFe_2O_4$ double-shell microspheres showed a response to acetone at 206 °C, which is mainly ascribed to their unique morphology [16]. Some researchers also found that Ag-activated hollow spheres of $ZnFe_2O_4$ exhibited an excellent acetone gas-sensing performance at 175 °C [17]. Moreover, $ZnFe_2O_4/ZnO$ composites showed an excellent response and recovery performance, which was attributed to their nanostructure and synergistic effects in the heterostructures. This will enable corresponding gas sensors to accurately detect and monitor acetone vapor in real-time. In this view, compounding with certain organic or inorganic material could improve the gas sensing properties of $ZnFe_2O_4$ [18,19].

As a novel 2D carbon-based material, graphene has a unique structure and distinguished properties. Plenty of works are in progress to investigate the applications of graphene or its derivatives in the field of gas sensing [20,21], including room temperature CO_2 gas sensors and room temperature double-layer graphene NO_2 gas sensors prepared by deposition processes [22,23]. Furthermore, the combination of metal oxides with graphene or its derivatives can enhance the gas sensing capability by improving the adsorption/desorption ability of the incorporated molecules, the transfer of carriers and the formation of local heterojunctions [24-28]. An optimum ratio of the composition and the fine nanostructure will contribute to obtaining better gas-sensing properties. A gas sensor with 3 wt % reduced graphene oxide (rGO) incorporated into In_2O_3 showed a rapid response, an improved stability and a low limit of detection of NO_2 (10 ppb) [29]. ZnO_{1-x}/rGO composites with 2 wt % rGO had enhanced gas sensing properties compared with pure ZnO, as indicated by an enhanced sensitivity and an improved response/recovery speed [30]. It has been proved that coupling or compounding metal oxides with graphene enhances the electronic characteristics and the gas sensing properties. Furthermore, 0.125 wt % graphene-$ZnFe_2O_4$ was prepared by a solvothermal method, and the corresponding gas sensor exhibited a fine response to 10–100 ppm acetone at 275 °C [31]. A hybrid sensor made of $ZnFe_2O_4$/graphene quantum dots showed a fine

sensing response to acetone at low temperature, even at room temperature [32].

Hence, with the aim to fabricate a high-performance acetone gas sensor, we prepared hollow spheres of $ZnFe_2O_4$ and $ZnFe_2O_4/rGO$ composites using a one-pot solvothermal method followed by a high-temperature heat treatment process in an inert atmosphere. The nanostructure, the micromorphology and the acetone sensing performance of all samples were discussed. Moreover, the optimized rGO mixing ratio and the operating temperature have been determined as 0.5 wt % and 200 °C, respectively.

Experimental
Materials
Aqueous dispersion solution of single-layer graphene oxide (GO) particles with average diameters of less than 500 nm and thicknesses of 0.8–1.2 nm (purity: 99%, concentration: 0.5 mg/mL) was purchased from Nanjing XFNANO Materials Technology Co., Ltd (Nanjing, China). Isopropanol (analytical degree) was obtained from Jiangsu Qiangsheng Functional Chemistry Co., Ltd (Suzhou, China). All other reagents (analytical degree) were purchased from Sinopharm Chemical Reagent Co., Ltd (Shanghai, China).

Samples synthesis
Hollow spheres of pure $ZnFe_2O_4$ and $ZnFe_2O_4/rGO$ composites were prepared via a simple solvothermal method followed by a high-temperature heat treatment process in an inert atmosphere. Firstly, the aqueous dispersion solution of GO (0.5 mg/mL) was further treated with ultrasound for 2 h. Then, different amounts of the GO solution (0, 0.242, 0.602, 1.205 and 2.410 mL) were added to the homogeneous solution of isopropanol (30 mL) and glycerol (8 mL) under slow stirring. Secondly, 0.1098 g $Zn(CH_3COO)_2 \cdot 2H_2O$ and 0.4042 g $Fe(NO_3)_3 \cdot 9H_2O$ were dissolved in the obtained homogeneous solution under magnetic stirring for 1 h. Subsequently, the mixed solutions were transferred into a Teflon-lined stainless-steel autoclave (50 mL), and then maintained at 180 °C for 12 h. After natural cooling to room temperature, the obtained suspensions were four times centrifuged using deionized water and anhydrous ethanol and dried at 75 °C for 12 h. Ultimately, these precursors were placed in an argon atmosphere, annealed at 400 °C for 2 h with a heating rate of 5 °C/min to reduce GO to rGO [33,34], and five samples were obtained: hollow spheres of pure $ZnFe_2O_4$ and $ZnFe_2O_4/rGO$ composite spheres with 0.1, 0.25, 0.5 and 1 wt % of rGO.

Characterization methods
The crystal phases of pure $ZnFe_2O_4$ and the $ZnFe_2O_4/rGO$ composites were characterized by X-ray diffraction (XRD,

Bruker D8 Advance) using Cu Kα radiation at room temperature. The 2θ range was 10−80°, and the scanning rate was 5°·min^{-1}. The microscopic morphology and the size of all samples were observed using a field-emission scanning electron microscope equipped with an energy-dispersive spectrometer (FESEM, Hitachi S4800). The nanostructure of the products was examined by transmission electron microscopy (TEM, JEM-2100). High-resolution TEM (HRTEM) and energy-dispersive X-ray (EDX) elemental mappings were recorded using a field-emission transmission electron microscope (Tecnai G2 F30 S-TWIN, FEI).

Fabrication and sensing test of gas sensors

The hollow spheres of pure $ZnFe_2O_4$ or $ZnFe_2O_4$/rGO powder were mixed with deionized water to obtain a paste, which was then manually uniformly coated onto an Al_2O_3 ceramic plate (C-MAC Micro Technology Company, Belgium) equipped with heating electrodes (Pt) and gold electrodes (Au) to fabricate sensing films. Subsequently, the sensors were dried at 120 °C for 12 h, and after further aging for 24 h at 180 °C, a series of $ZnFe_2O_4$/rGO gas sensors (different mass content of rGO: 0, 0.1, 0.25, 0.5 and 1 wt %) were obtained. Figure 1 is the schematic image of an electric circuit equivalent to the sensor system along with the dimensions of the corresponding $ZnFe_2O_4$/rGO gas sensor. The operating temperature of the sensors was adjusted by means of the applied voltage. Further details of the testing system were shown in our previous works [17,30]. The target gas was collected in a poly(methyl methacrylate) (PMMA) chamber (volume: 50 L), the volume of which was calibrated using the following Equation 1:

$$V_x = \frac{V \times c \times M}{22.4 \times \rho \times P} \times 10^{-6} \qquad (1)$$

V_x is the volume of the liquid (μL), c is the concentration of the gas to be allocated (ppm), V is the volume of the collection vessel (mL), M is the molecular weight of the substance (g), P

is the purity of the liquid and ρ is the density of the liquid (g/cm^3). In addition, the response of the sensors was defined as $S = R_a/R_g$, where R_a and R_g are the resistance values of the sensors in air and in test gas, respectively. The response/recovery time is defined as the time required for a change of the resistance of 90%.

Results and Discussion
Samples characterization

The XRD patterns of the spheres of pure $ZnFe_2O_4$ and the four $ZnFe_2O_4$/rGO composites with different mass fractions of rGO are shown in Figure 2. All samples showed similar diffraction peaks, and according to the well-known diffraction pattern of $ZnFe_2O_4$ (JCPDS Card No. 22-1012), all the peaks of the five samples agree well with the spinel $ZnFe_2O_4$ structure. Hence, the introduction of rGO did not affect the spinel structure of $ZnFe_2O_4$. The characteristic peaks observed at 29.9°, 35.1°, 42.8°, 53.3°, 56.5° and 62.2° were attributed to the (220), (311), (400), (422), (511) and (440) crystal planes, respectively. Furthermore, the strong intensity of the diffraction peaks suggests that both the hollow spheres of pure $ZnFe_2O_4$ and of the $ZnFe_2O_4$/rGO composites were well crystallized. In addition, the characteristic peaks of rGO, that should be observed at about 24°, are not clearly identified in the patterns, which may be ascribed to the low mass fraction of rGO in the $ZnFe_2O_4$/rGO composites [35,36].

The surface morphology and the size of the hollow spheres of pure $ZnFe_2O_4$ and the $ZnFe_2O_4$/rGO composites with different rGO content were analyzed. Figure 3a and Figure 3b show that pristine particles in $ZnFe_2O_4$ powder have a spherical morphology. The mean diameters of the spheres were measured as 600–1000 nm using the ImageJ software. It is observed that the spheres of pure $ZnFe_2O_4$ are composed of small nanosheets. Furthermore, as shown in Figure 3, there is almost no change in the diameter of the $ZnFe_2O_4$/rGO composites when the rGO content is increased from 0 to 1 wt %. However, Figure 3d,
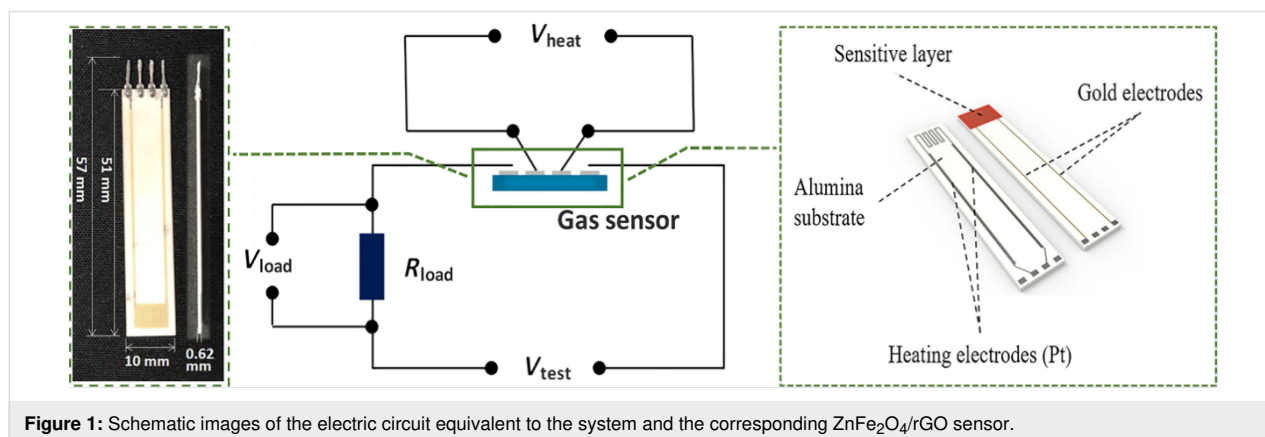

Figure 1: Schematic images of the electric circuit equivalent to the system and the corresponding $ZnFe_2O_4$/rGO sensor.
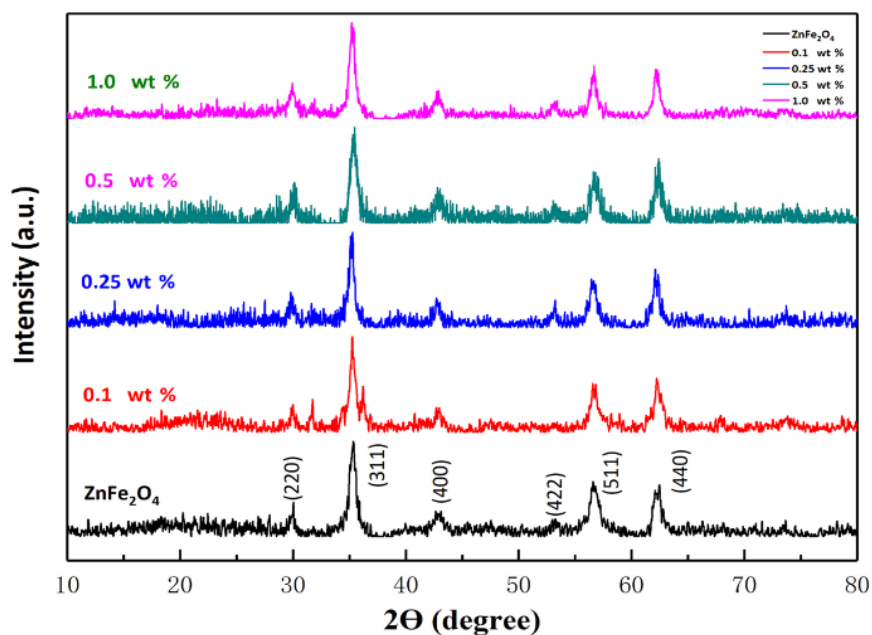
Figure 2: XRD patterns of the synthesized hollow spheres of pure $ZnFe_2O_4$ and the different $ZnFe_2O_4$/rGO composites.

Figure 3f, Figure 3h and Figure 3j show that when the rGO content exceeds 0.25 wt %, there are more $ZnFe_2O_4$ spheres which are composed of small nanoparticles instead of nanosheets. This deformation of the self-assembled structure of the nanosheets may be ascribed to the introduction of more water to the organic solvent when increasing the volume of the aqueous GO dispersion [37,38] or to the low mass fraction of rGO in the $ZnFe_2O_4$/rGO composites [17,39].

We analyzed the actual composition of the spheres by energy-dispersive X-ray spectroscopy (EDS). As shown in Figure 4, the weight percentage of carbon in the spheres of $ZnFe_2O_4$/rGO with 0.5 and 1 wt % rGO was determined as 1.17 and 1.53%, respectively. The obtained percentage is higher than theoretically predicted, which may be due to a contamination arising from the carbon-containing electrically conductive adhesive or another source of carbon in the sample stage or on the sample surface. Still, the actual quantities derived by EDX are basically consistent with the theoretical quantities.

Figure 5 shows the TEM images of GO and the hollow spheres of pure $ZnFe_2O_4$ and the four $ZnFe_2O_4$/rGO composites. The wrinkles in Figure 5a indicate the two-dimensional structure of GO. Figure 5b–f further shows that the samples made of pure $ZnFe_2O_4$ and $ZnFe_2O_4$/rGO all have the structure of hollow spheres. Furthermore, with increasing rGO content in the $ZnFe_2O_4$/rGO nanomaterial, the surface of the $ZnFe_2O_4$ spheres becomes more regular and smooth, which is consistent with the FESEM images.

A further analysis of the nanostructure of the $ZnFe_2O_4$/rGO sample with 0.5 wt % rGO was carried out using TEM and HRTEM (Figure 6). As obvious from Figure 6a and Figure 6b, the $ZnFe_2O_4$ spheres are uniformly distributed on the rGO nanosheets. The HRTEM image shown in Figure 6c shows two planes with lattice spacing of ca. 0.25 and 0.21 nm, which correspond to the (311) and the (400) planes of the spinel $ZnFe_2O_4$ crystals. In addition, the angle of the two is measured as 25.24°, which is consistent with computations of the crystal structure. Moreover, the inserted fast Fourier transform (FFT) image reveals the typical hexagonal diffraction ring of rGO. As shown in Figure 6d, the selected area diffraction (SAED) pattern shows a series of distinct diffraction rings, which can be readily indexed to the (220), (311), (400), (422), (511) and (440) planes of the spinel $ZnFe_2O_4$ crystal, in line with the above XRD results. Moreover, the SAED pattern exhibits the polycrystalline nature of the 0.5 wt % $ZnFe_2O_4$/rGO composite. Furthermore, the composition of the sample was analyzed by high-angle annular dark-field imaging scanning transmission electron microscopy (HAADF-STEM) and EDS. The element mappings in Figure 6e reveal the existence of C, Zn, Fe and O in the 0.5 wt % $ZnFe_2O_4$/rGO spheres confirming the formation of a composite structure with hollow spheres of $ZnFe_2O_4$ distributed on the carbon matrix.

Gas sensing performance

The response of the fabricated gas sensors to 10 ppm acetone as a function of the operating temperature (150–225 °C) is shown in Figure 7. All the $ZnFe_2O_4$/rGO sensors show an enhanced
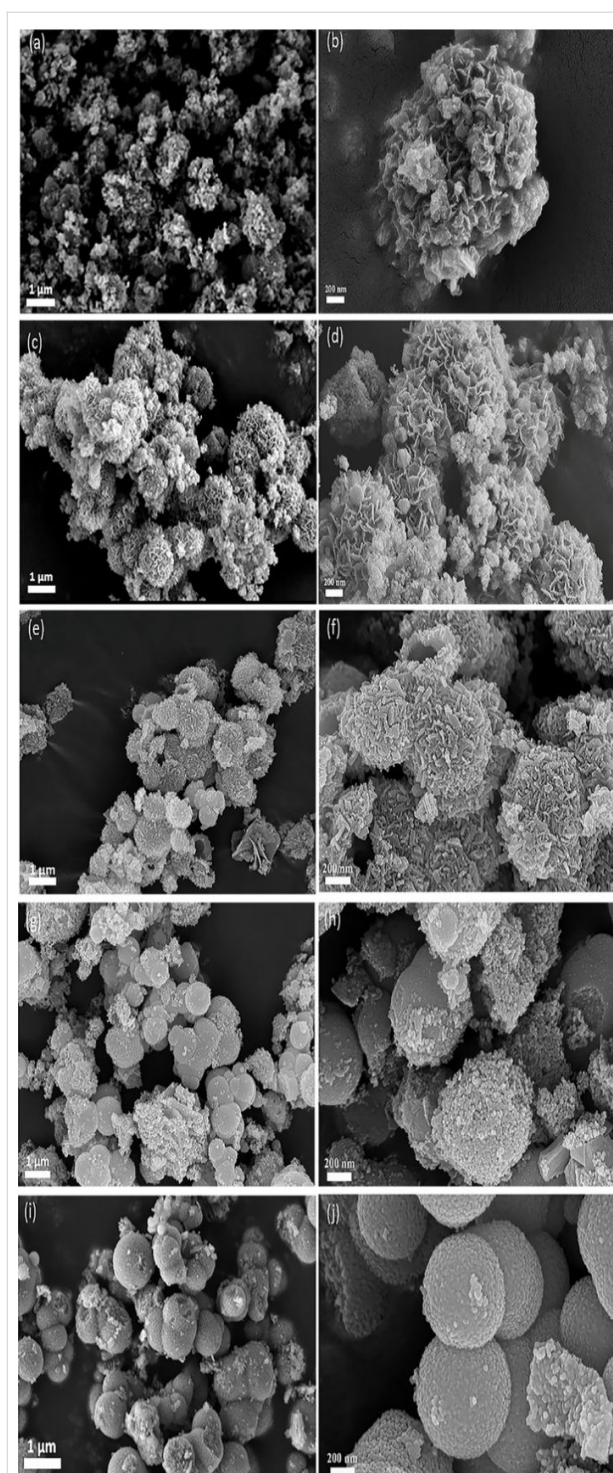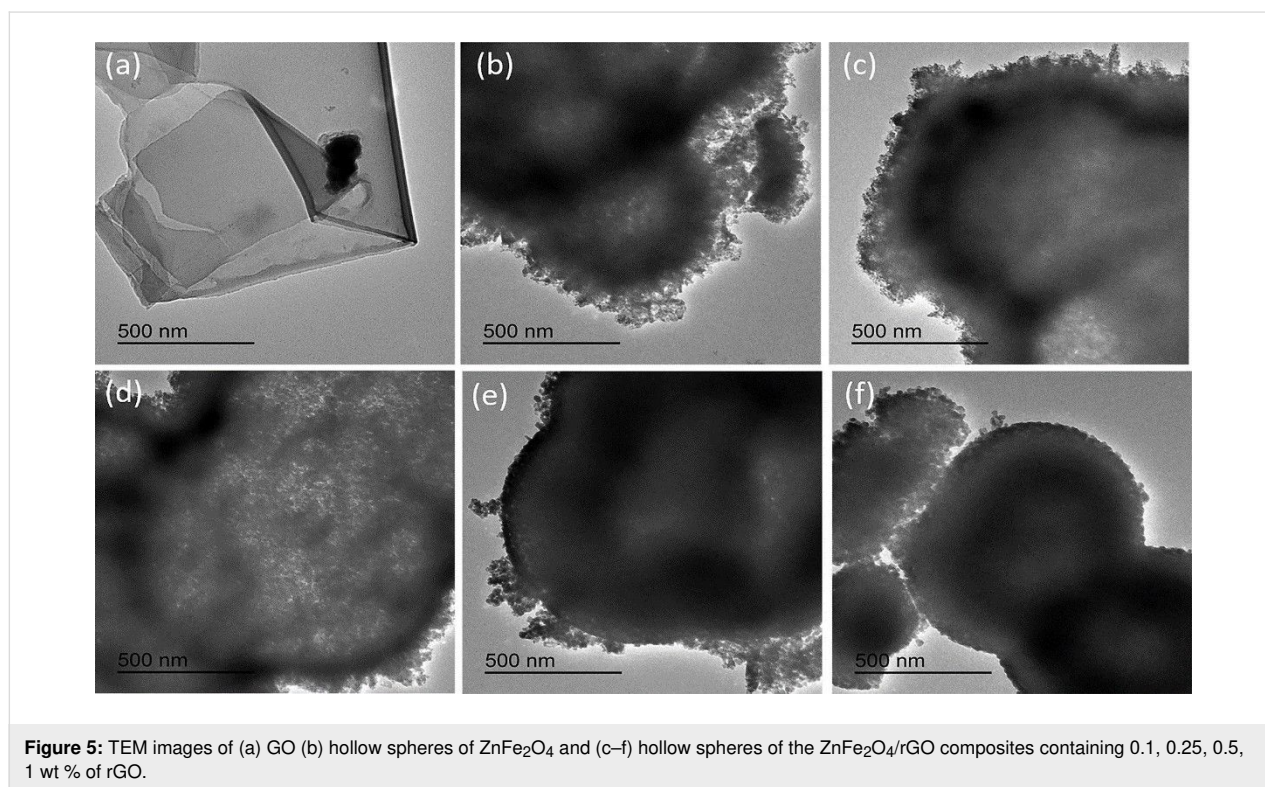
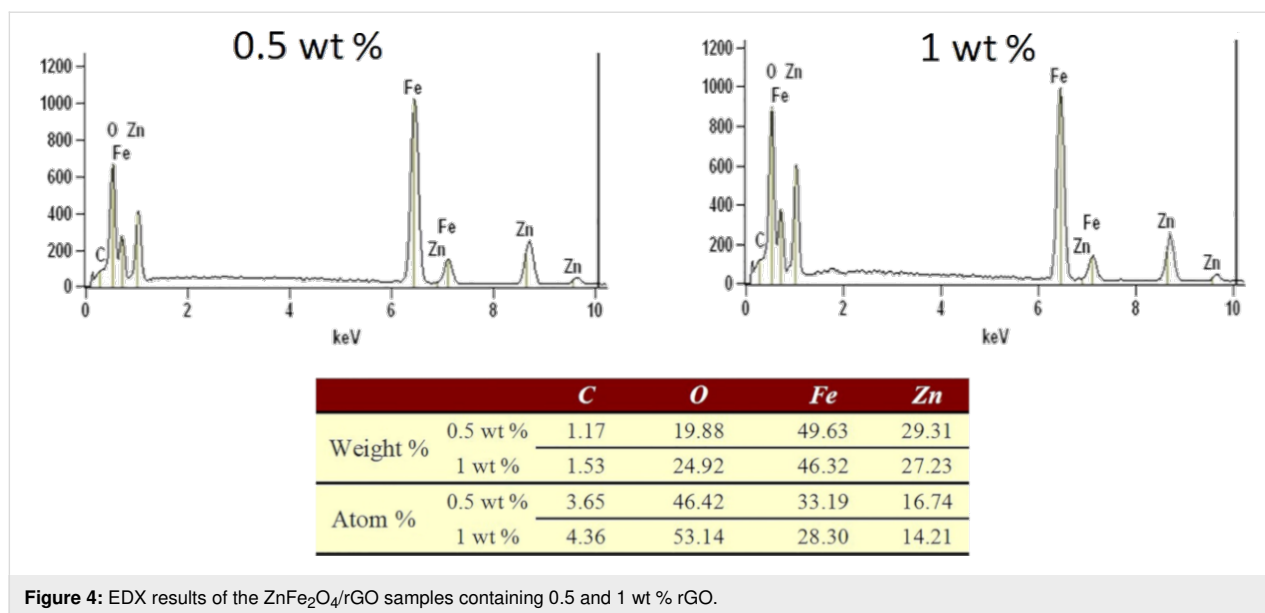**Figure 3:** FESEM images of the hollow spheres made of (a, b) pure $ZnFe_2O_4$ and composite $ZnFe_2O_4$/rGO with an rGO percentage of (c, d) 0.1, (e, f) 0.25, (g, h) 0.5 and (i, j) 1 wt %.

response when the temperature is increased from 150 to 200 °C, while for the pure $ZnFe_2O_4$ sensor the response has a maximum at 175 °C. This tendency is ascribed to the higher surface activation energy at elevated temperature. As a result, the activa-

tion energy barrier of surface reactions with the target gas molecules is more easily overcome, resulting in an increased response [40,41]. At 200 °C, the 0.5 wt % $ZnFe_2O_4$/rGO sensor shows the highest response of 8.18. At a temperature of 225 °C, the responses decrease quickly, most likely due to the faster motion of the acetone molecules at elevated temperature. When moving faster, the adsorption of acetone at the sensor surface is less efficient, and the surface reaction of acetone and the chemisorbed oxygen ions is decelerated. Hence, the optimal operating temperature for the $ZnFe_2O_4$/rGO sensors is determined as 200 °C.

Figure 8a shows the dynamic response of the five sensors to 0.8–100 ppm acetone at 200 °C. It can be observed that the response increases significantly for the samples with higher content of rGO. Notably, the $ZnFe_2O_4$/rGO sensor containing 0.5 wt % of rGO showed an improved acetone sensing performance, the response to 0.8 and 10 ppm acetone was 1.50 and 8.18, while the corresponding values of the pure $ZnFe_2O_4$ sensor were 1.09 and 3.20. However, the response decreases with the increase of the rGO content from 0.5 to 1 wt %, which may be explained as follows. The addition of a large amount of the aqueous dispersion of GO to the organic solvent, in which the reaction occurrs, affects the formation of the $ZnFe_2O_4$ hollow spheres [17,39], resulting in a limitation of surface reactions. In addition, as shown in Figure 8b, the response of the sensors to 25–100 ppm acetone was also probed employing the same experimental conditions. The $ZnFe_2O_4$/rGO sensor with 0.5 wt % rGO still exhibits the best sensing performance. As shown in Figure 8c and Figure 8d, the sensor of pure $ZnFe_2O_4$ and the $ZnFe_2O_4$/rGO sensor with 0.5 wt % rGO both showed a good short term stability. Moreover, the 0.5 wt % $ZnFe_2O_4$/rGO sensor showed a shorter response/recovery time to 10 ppm acetone at 200 °C. The response time has been measured as 60 s for the pure $ZnFe_2O_4$ sensor and only 23 s for the 0.5 wt % $ZnFe_2O_4$/rGO sensor.
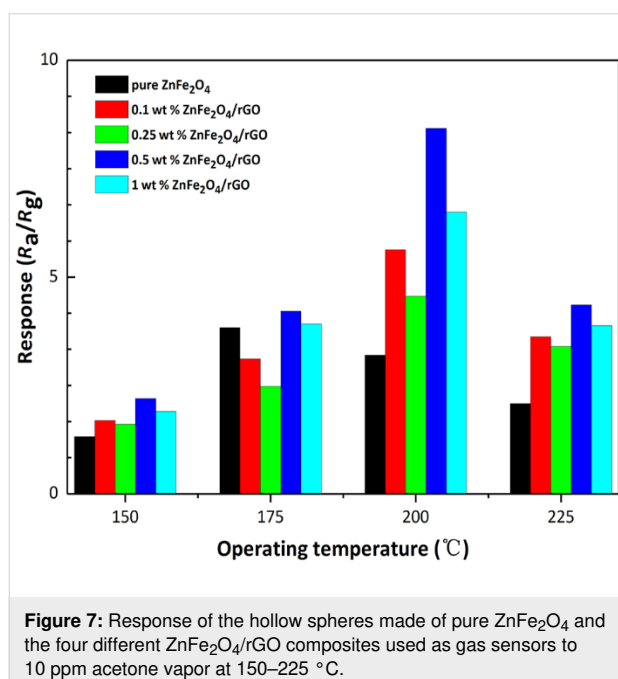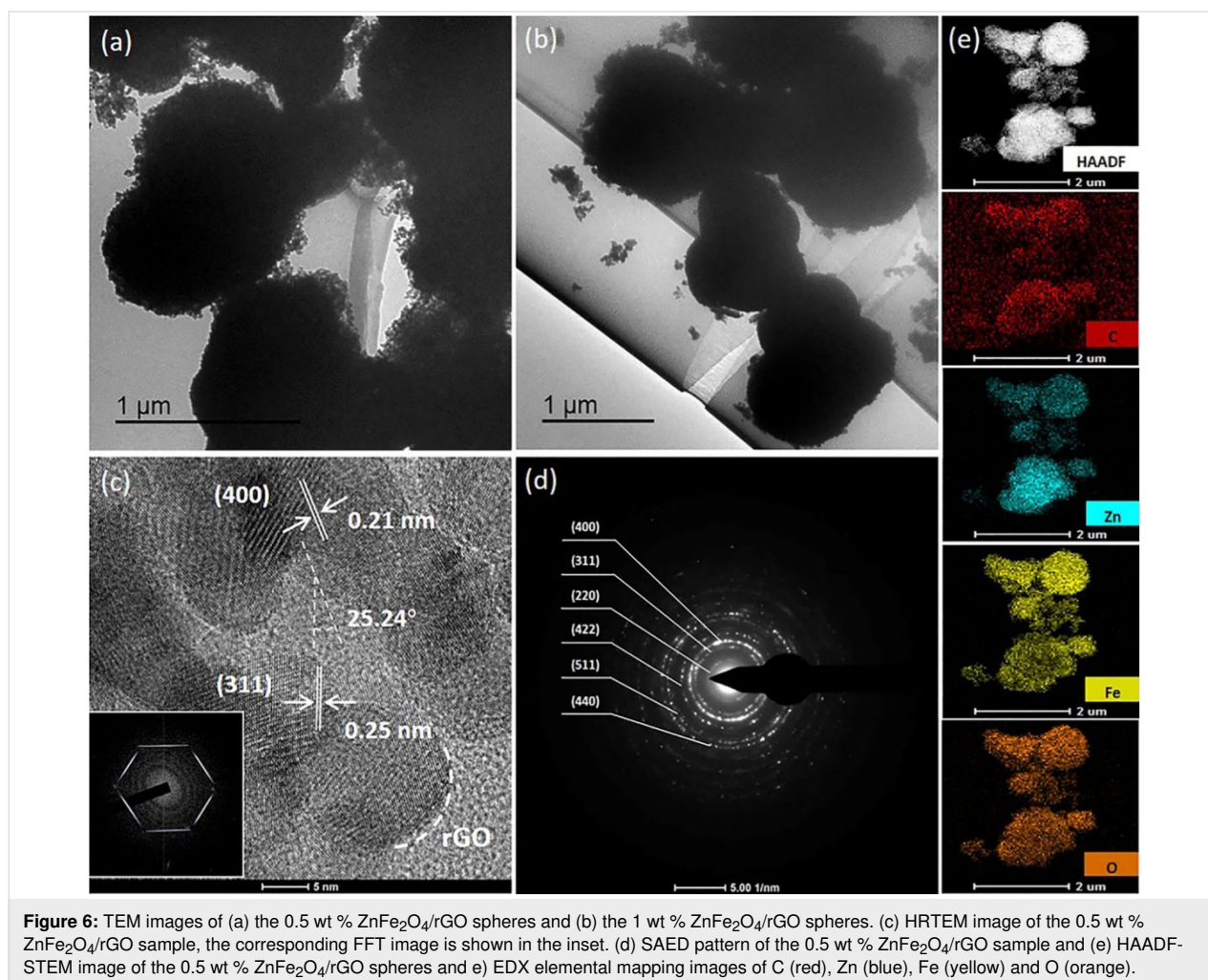
Figure 9 shows the responses of the pure $ZnFe_2O_4$ sensor and the 0.5 wt % $ZnFe_2O_4$/rGO sensor to acetone at different concentration at 200 °C and the corresponding fitting data. The results demonstrate that the response of the hollow spheres made of pure $ZnFe_2O_4$ and of $ZnFe_2O_4$/rGO with 0.5 wt % rGO are more intense at higher concentration of acetone. Moreover, it is obvious that the linear response of the 0.5 wt % $ZnFe_2O_4$/rGO sensor has a steeper slope indicating an improved potential for quantitative gas analysis compared to the gas sensor of pure $ZnFe_2O_4$. For this composite gas sensor, the response to 1 ppm acetone is calculated to be 2.19, while the response of the pure $ZnFe_2O_4$ sensor to 5 ppm was only 1.83. Thus, the $ZnFe_2O_4$/rGO gas sensor with 0.5 wt % has a lower detection limit and shows an improved response. Furthermore, the

Figure 4: EDX results of the $ZnFe_2O_4$/rGO samples containing 0.5 and 1 wt % rGO.

		C	*O*	*Fe*	*Zn*
Weight %	0.5 wt %	1.17	19.88	49.63	29.31
	1 wt %	1.53	24.92	46.32	27.23
Atom %	0.5 wt %	3.65	46.42	33.19	16.74
	1 wt %	4.36	53.14	28.30	14.21

Figure 5: TEM images of (a) GO (b) hollow spheres of $ZnFe_2O_4$ and (c–f) hollow spheres of the $ZnFe_2O_4$/rGO composites containing 0.1, 0.25, 0.5, 1 wt % of rGO.

0.5 wt % $ZnFe_2O_4$/rGO gas sensor showed a better performance of acetone sensing at a lower temperature than any previously reported $ZnFe_2O_4$-based gas sensors (Table 1).
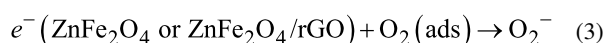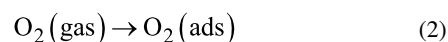
The selectivity of gas sensors is an important issue for practical applications. Herein, ethanol, methanol and formaldehyde were selected to measure the selectivity of the 0.5 wt % $ZnFe_2O_4$/rGO gas sensor at 200 °C. As shown in Figure 10, the responses

to 10 ppm acetone, ethanol, methanol and formaldehyde were 8.18, 2.76, 2.05 and 1.31, respectively. It is obvious that the most intense response of the 0.5 wt % $ZnFe_2O_4$/rGO gas sensor corresponds to acetone. It is about three times more pronounced than the response to ethanol. The results reveal the excellent selectivity of the composite sensor for acetone. These findings are similar to the results of several previously reported works [45-47].

Figure 6: TEM images of (a) the 0.5 wt % $ZnFe_2O_4$/rGO spheres and (b) the 1 wt % $ZnFe_2O_4$/rGO spheres. (c) HRTEM image of the 0.5 wt % $ZnFe_2O_4$/rGO sample, the corresponding FFT image is shown in the inset. (d) SAED pattern of the 0.5 wt % $ZnFe_2O_4$/rGO sample and (e) HAADF-STEM image of the 0.5 wt % $ZnFe_2O_4$/rGO spheres and e) EDX elemental mapping images of C (red), Zn (blue), Fe (yellow) and O (orange).

Figure 7: Response of the hollow spheres made of pure $ZnFe_2O_4$ and the four different $ZnFe_2O_4$/rGO composites used as gas sensors to 10 ppm acetone vapor at 150–225 °C.

Acetone sensing mechanism

The most accepted explanation of the acetone sensing mechanism of $ZnFe_2O_4$, which is an n-type semiconductor, is described as a reaction at the gas–solid interface. When the $ZnFe_2O_4$ gas sensor is placed in air at 200 °C, the adsorbed oxygen atoms capture free electrons from the conduction band to form adsorbed oxygen anions (O_2^-, O^-). In $ZnFe_2O_4$, an electron depletion layer is left, which will result in an increase of the resistance. Upon exposure to acetone, the acetone molecules will adsorb to the surface of $ZnFe_2O_4$ and react with the adsorbed O_2^- and O^- anions at the $ZnFe_2O_4$ grain boundaries. Subsequently, the electrons will be released back to the conduction band and the resistance will decrease again. The whole process can be described by Equations 2–5 [31,48].
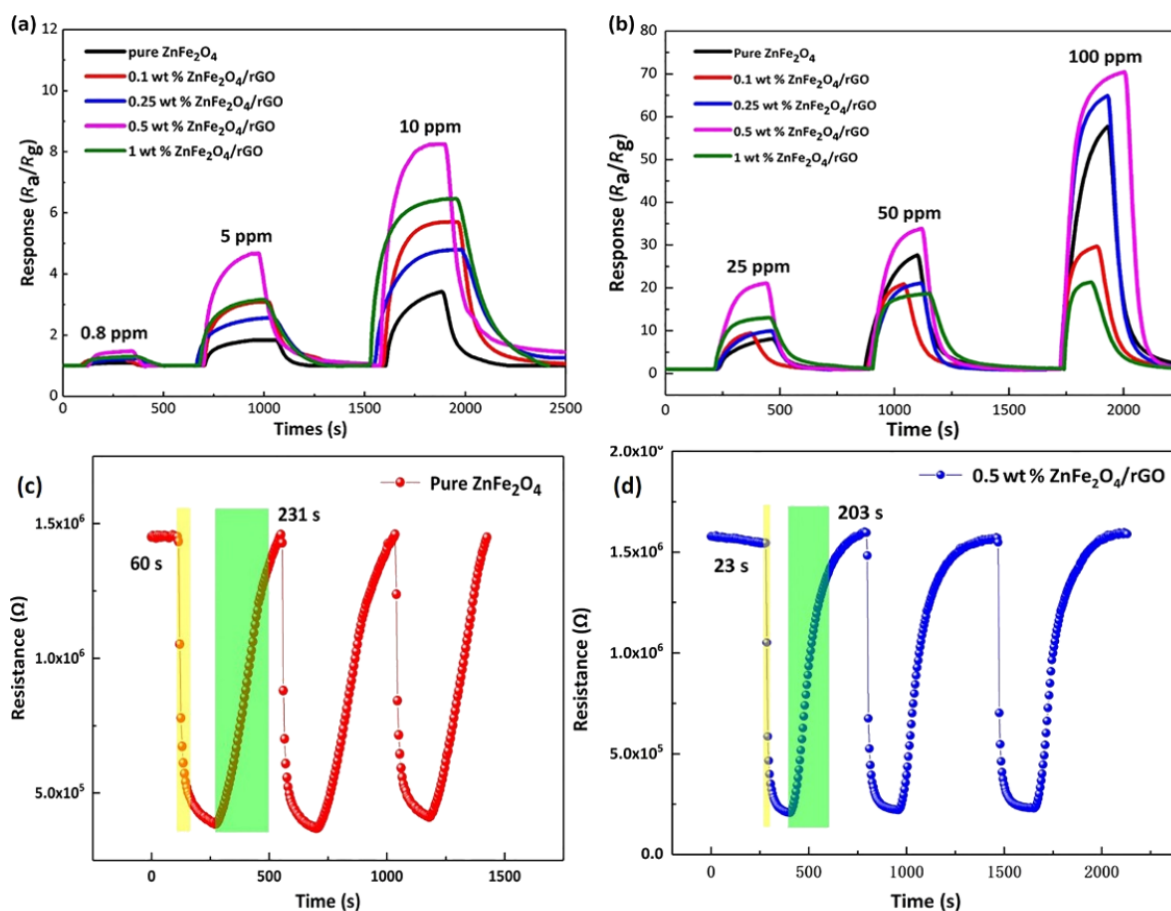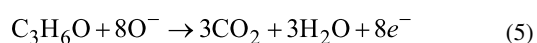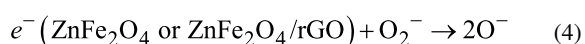
$$O_2\left(gas\right) \rightarrow O_2\left(ads\right) \tag{2}$$

$$e^-\left(ZnFe_2O_4 \text{ or } ZnFe_2O_4/rGO\right) + O_2\left(ads\right) \rightarrow O_2^- \tag{3}$$

Figure 8: Dynamic response/recovery curves of the pure $ZnFe_2O_4$ and the four $ZnFe_2O_4$/rGO gas sensors to (a) 0.8–10 ppm and (b) 25–100 ppm acetone at 200 °C. (c, d) The short term stability and the response/recovery time of the pure $ZnFe_2O_4$ and the 0.5 wt % $ZnFe_2O_4$/rGO sensors to 10 ppm acetone measured in three cycles.

Table 1: Comparison of the acetone sensing performance of various reported sensors based on different materials.

Materials	Operating temperature (°C)	Conc. (ppm)	Response	LOD[a] (ppm)	Ref.
NiO-ZnO hybrid	260	200	7.5	5	[41]
$ZnFe_2O_4$ nanosheet-assembled hollow spheres	215	20	9.8	1	[42]
$ZnO/ZnFe_2O_4$ hollow spheres	280	50	5.2	10	[43]
1 wt % rGO/α-Fe_2O_3	225	10	2.9	5	[25]
1 wt % RGO-$CdFe_2O_4$	270	10	20.7	0.01	[44]
0.125 wt % $RGO/ZnFe_2O_4$	275	10	4.0	1	[31]
$ZnFe_2O_4$-graphene quantum dots	room temperature	10	3.2	5	[32]
0.5 wt % $ZnFe_2O_4$/rGO hollow spheres	200	10	8.2	0.8	this work

[a]LOD represents the limit of detection.

$$e^- \left(ZnFe_2O_4 \text{ or } ZnFe_2O_4/rGO \right) + O_2^- \rightarrow 2O^- \quad (4)$$

$$C_3H_6O + 8O^- \rightarrow 3CO_2 + 3H_2O + 8e^- \quad (5)$$

In this work, the 0.5 wt % $ZnFe_2O_4$/rGO gas sensor showed an enhanced acetone sensing performance compared to the sensor of pure $ZnFe_2O_4$ due to the unique hollow structure of the $ZnFe_2O_4$ spheres and the excellent electrical properties of the 2D-rGO nanosheets [49,50]. More precisely, the enhanced acetone sensing properties may be attributed to several aspects.
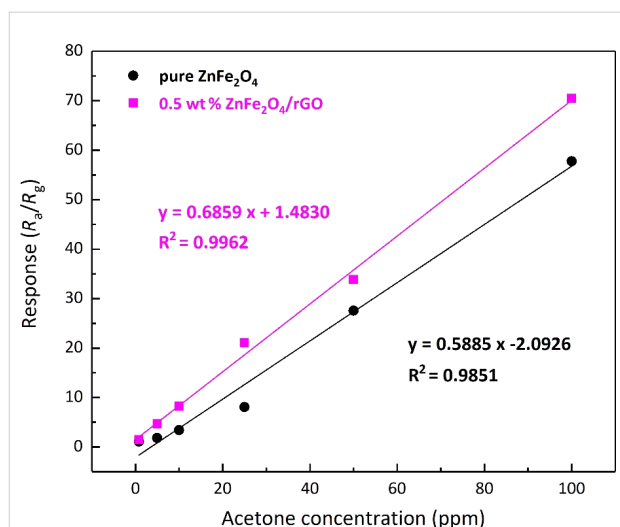
Figure 9: Linear response of (a) the hollow spheres of pure $ZnFe_2O_4$ and (b) of $ZnFe_2O_4$/rGO with 0.5 wt % rGO to acetone at different concentration.

First, the sensing mechanism is based on the mentioned reaction at the gas–solid interface. Second, an appropriate content of rGO can improve the electron mobility inside the composites, which is helpful for the interface reaction [24,51]. Third, as shown in Figure 11a, the Fermi energy levels equalize when two semiconducting systems are in contact via the transfer of carriers. Consequently, heterojunctions and regions of electron depletion will be formed at the interface between rGO, which is

a p-type semiconductor, and $ZnFe_2O_4$, an n-type semiconductor. In addition, there will also exist a potential barrier at the grain boundaries. In Figure 11b, when air is introduced, the resistance of the sensor will decrease as a result of the construction of the depletion layers and the potential barriers at the grain boundaries (see also Equations 2–5). When acetone is introduced, the resistance of the sensor will decrease again because of the contraction of the depletion layers and the potential barriers [19,25,52,53]. As a result, a sensing signal is obtained.

Conclusion

In this work, the capability of different $ZnFe_2O_4$ sensors to detect acetone at low-ppm level was improved by incorporation of rGO. The rGO mass fraction of the $ZnFe_2O_4$/rGO spheres was 0, 0.1, 0.25, 0.5 and 1 wt %, respectively. Upon introduction of rGO, the size and the hollow structure of the sphere were not affected, while the surface morphology was modified and became more regular. The $ZnFe_2O_4$/rGO sensor containing 0.5 wt % rGO showed a sensitive linear response to a low concentration of acetone at 200 °C and exhibited a good selectivity. The response of the 0.5 wt % $ZnFe_2O_4$/rGO sensor to 10 ppm acetone was 8.18, which is about 2.5 times higher than that of the corresponding sensor made of pure $ZnFe_2O_4$. Therefore, this sensor shows great promise for detecting acetone at low concentration (ppm). It is a suitable candidate for the nondestructive diagnosis of diabetes by means of concentration measurements of exhaled acetone vapor if the sensitivity and the response speed to acetone at ppb-level are further improved.
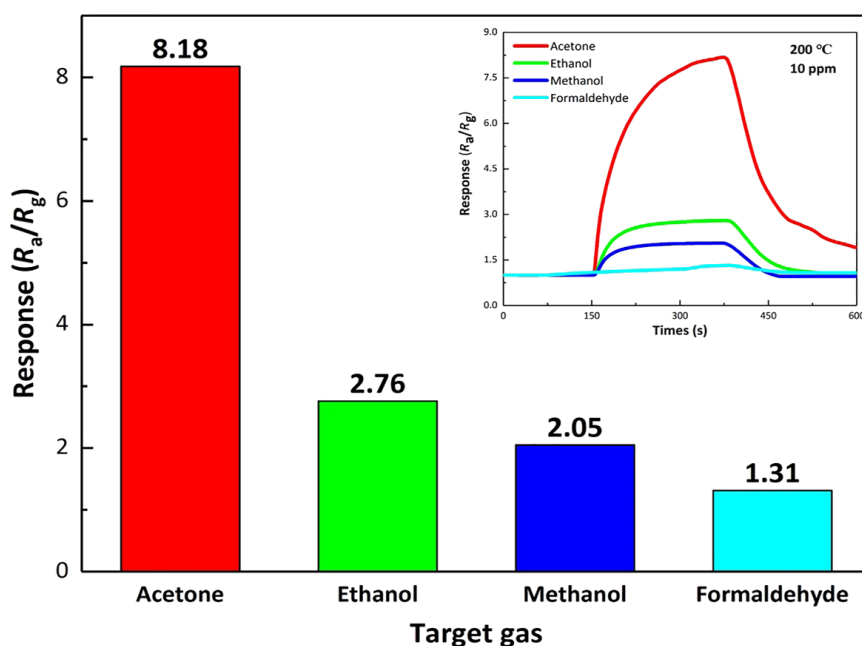

Figure 10: Response of the 0.5 wt % $ZnFe_2O_4$/rGO sensor to 10 ppm of acetone, ethanol, methanol and formaldehyde at 200 °C.

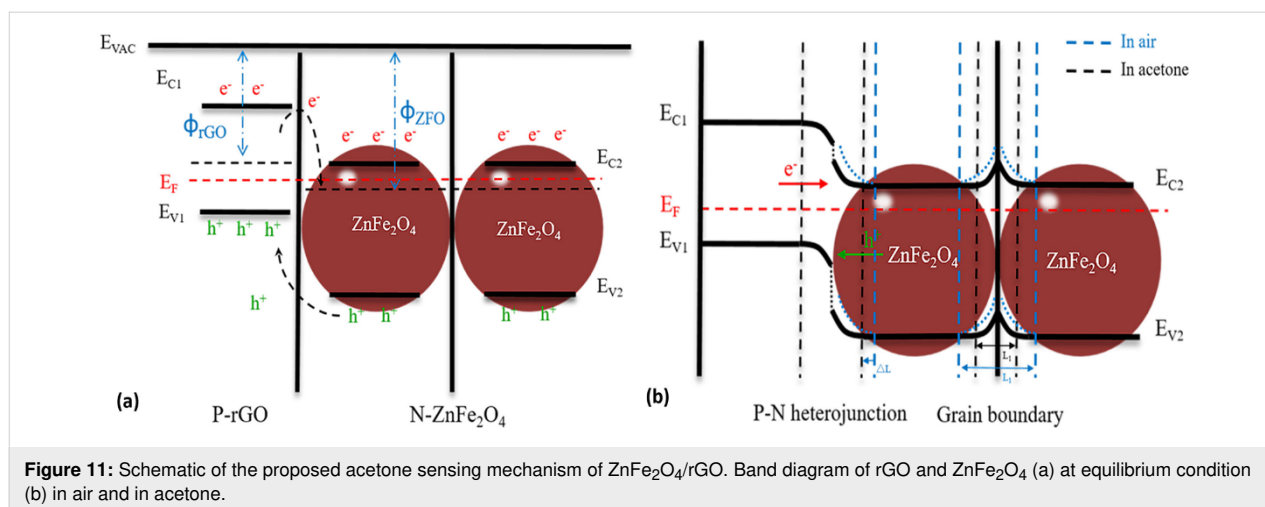**Figure 11:** Schematic of the proposed acetone sensing mechanism of ZnFe$_2$O$_4$/rGO. Band diagram of rGO and ZnFe$_2$O$_4$ (a) at equilibrium condition (b) in air and in acetone.

References

1. Wang, L.; Teleki, A.; Pratsinis, S. E.; Gouma, P. I. *Chem. Mater.* **2008,** *20,* 4794–4796. doi:10.1021/cm800761e

2. Liu, T.; Li, W.; Zhang, Y.; Hao, X.; Zhang, Y.; Liang, X.; Liu, F.; Liu, F.; Yan, X.; Gao, Y.; Zhang, T.; Zhang, C.; Lu, G. *Sens. Actuators, B* **2019,** *284,* 751–758. doi:10.1016/j.snb.2018.12.136

3. Jia, Q.; Ji, H.; Zhang, Y.; Chen, Y.; Sun, X.; Jin, Z. *J. Hazard. Mater.* **2014,** *276,* 262–270. doi:10.1016/j.jhazmat.2014.05.044

4. Xiao, T.; Wang, X.-Y.; Zhao, Z.-H.; Li, L.; Zhang, L.; Yao, H.-C.; Wang, J.-S.; Li, Z.-J. *Sens. Actuators, B* **2014,** *199,* 210–219. doi:10.1016/j.snb.2014.04.015

5. Hussain, T.; Vovusha, H.; Umer, R.; Ahuja, R. *Appl. Surf. Sci.* **2018,** *456,* 711–716. doi:10.1016/j.apsusc.2018.06.155

6. Zhang, X.; Xu, G.; Wang, H.; Cui, H.; Zhan, X.; Wang, X. *Powder Technol.* **2019,** *344,* 183–189. doi:10.1016/j.powtec.2018.12.020

7. Imran, M.; Rashid, S. S. A. A. H.; Sabri, Y.; Motta, N.; Tesfamichael, T.; Sonar, P.; Shafiei, M. *J. Mater. Chem. C* **2019,** *7,* 2961–2970. doi:10.1039/c8tc05982a

8. Maziarz, W.; Kusior, A.; Trenczek-Zajac, A. *Beilstein J. Nanotechnol.* **2016,** *7,* 1718–1726. doi:10.3762/bjnano.7.164

9. Singh, G.; Virpal; Singh, R. C. *Sens. Actuators, B* **2019,** *282,* 373–383. doi:10.1016/j.snb.2018.11.086

10. Ma, R.-J.; Zhao, X.; Zou, X.; Li, G.-D. *J. Alloys Compd.* **2018,** *732,* 863–870. doi:10.1016/j.jallcom.2017.10.224

11. Zhang, J.; Lu, H.; Yan, C.; Yang, Z.; Zhu, G.; Gao, J.; Yin, F.; Wang, C. *Sens. Actuators, B* **2018,** *264,* 128–138. doi:10.1016/j.snb.2018.02.026

12. Singkammo, S.; Wisitsoraat, A.; Sriprachuabwong, C.; Tuantranont, A.; Phanichphant, S.; Liewhiran, C. *ACS Appl. Mater. Interfaces* **2015,** *7,* 3077–3092. doi:10.1021/acsami.5b00161

13. Zhang, D.; Zong, X.; Wu, Z.; Zhang, Y. *ACS Appl. Mater. Interfaces* **2018,** *10,* 32631–32639. doi:10.1021/acsami.8b08493

14. Zhang, D.; Wu, Z.; Zong, X.; Zhang, Y. *Sens. Actuators, B* **2018,** *274,* 575–586. doi:10.1016/j.snb.2018.08.001

15. Zhang, J.; Song, J.-M.; Niu, H.-L.; Mao, C.-J.; Zhang, S.-Y.; Shen, Y.-H. *Sens. Actuators, B* **2015,** *221,* 55–62. doi:10.1016/j.snb.2015.06.040

16. Qu, F.; Shang, W.; Thomas, T.; Ruan, S.; Yang, M. *Sens. Actuators, B* **2018,** *265,* 625–631. doi:10.1016/j.snb.2018.03.108

17. Zhang, C.; Wu, Q.; Zheng, B.; You, J.; Luo, Y. *Ceram. Int.* **2018,** *44,* 20700–20707. doi:10.1016/j.ceramint.2018.08.064

18. Wu, K.; Li, J.; Zhang, C. *Ceram. Int.* **2019,** *45,* 11143–11157. doi:10.1016/j.ceramint.2019.03.086

19. Van Hoang, N.; Hung, C. M.; Hoa, N. D.; Van Duy, N.; Park, I.; Van Hieu, N. *Sens. Actuators, B* **2019,** *282,* 876–884. doi:10.1016/j.snb.2018.11.157

20. Zhang, D.; Wu, Z.; Zong, X. *Sens. Actuators, B* **2019,** *288,* 232–242. doi:10.1016/j.snb.2019.02.093

21. Zhang, D.; Yang, Z.; Wu, Z.; Dong, G. *Sens. Actuators, B* **2019,** *283,* 42–51. doi:10.1016/j.snb.2018.11.133

22. Muhammad Hafiz, S.; Ritikos, R.; Whitcher, T. J.; Md. Razib, N.; Bien, D. C. S.; Chanlek, N.; Nakajima, H.; Saisopa, T.; Songsiriritthigul, P.; Huang, N. M.; Rahman, S. A. *Sens. Actuators, B* **2014,** *193,* 692–700. doi:10.1016/j.snb.2013.12.017

23. Seekaew, Y.; Phokharatkul, D.; Wisitsoraat, A.; Wongchoosuk, C. *Appl. Surf. Sci.* **2017,** *404,* 357–363. doi:10.1016/j.apsusc.2017.01.286

24. Sun, D.; Luo, Y.; Debliquy, M.; Zhang, C. *Beilstein J. Nanotechnol.* **2018,** *9,* 2832–2844. doi:10.3762/bjnano.9.264

25. Galstyan, V.; Comini, E.; Kholmanov, I.; Ponzoni, A.; Sberveglieri, V.; Poli, N.; Faglia, G.; Sberveglieri, G. *Beilstein J. Nanotechnol.* **2016,** *7,* 1421–1427. doi:10.3762/bjnano.7.133

26. Lee, H.-Y.; Heish, Y.-C.; Lee, C.-T. *J. Alloys Compd.* **2019,** *773,* 950–954. doi:10.1016/j.jallcom.2018.09.290

27. Zhang, D.; Liu, J.; Jiang, C.; Liu, A.; Xia, B. *Sens. Actuators, B* **2017,** *240,* 55–65. doi:10.1016/j.snb.2016.08.085

28. Zhang, D.; Liu, A.; Chang, H.; Xia, B. *RSC Adv.* **2015,** *5,* 3016–3022. doi:10.1039/c4ra10942b

29. Liu, J.; Li, S.; Zhang, B.; Wang, Y.; Gao, Y.; Liang, X.; Wang, Y.; Lu, G. *J. Colloid Interface Sci.* **2017,** *504,* 206–213. doi:10.1016/j.jcis.2017.05.053

30. Geng, X.; Lu, P.; Zhang, C.; Lahem, D.; Olivier, M.-G.; Debliquy, M.
    Sens. Actuators, B **2019,** *282,* 690–702. doi:10.1016/j.snb.2018.11.123
31. Liu, F.; Chu, X.; Dong, Y.; Zhang, W.; Sun, W.; Shen, L.
    Sens. Actuators, B **2013,** *188,* 469–474. doi:10.1016/j.snb.2013.06.065
32. Chu, X.; Dai, P.; Liang, S.; Bhattacharya, A.; Dong, Y.; Epifani, M.
    Phys. E (Amsterdam, Neth.) **2019,** *106,* 326–333.
    doi:10.1016/j.physe.2018.08.003
33. Kalantari Bolaghi, Z.; Masoudpanah, S. M.; Hasheminiasari, M.
    Mater. Res. Bull. **2019,** *115,* 191–195.
    doi:10.1016/j.materresbull.2019.03.024
34. Jung, M. W.; Kang, S. M.; Nam, K.-H.; An, K.-S.; Ku, B.-C.
    Appl. Surf. Sci. **2018,** *456,* 7–12. doi:10.1016/j.apsusc.2018.06.086
35. You, J.; Chen, X.; Zheng, B.; Geng, X.; Zhang, C.
    J. Therm. Spray Technol. **2017,** *26,* 728–734.
    doi:10.1007/s11666-017-0536-7
36. Shi, M.; Shen, J.; Ma, H.; Li, Z.; Lu, X.; Li, N.; Ye, M. *Colloids Surf., A*
    2012, *405,* 30–37. doi:10.1016/j.colsurfa.2012.04.031
37. Xu, C.; Wang, X.; Zhu, J. *J. Phys. Chem. C* **2008,** *112,* 19841–19845.
    doi:10.1021/jp807989b
38. Wu, S.; Li, X.; Xu, Y.; Wu, J.; Wang, Z.; Han, Y.; Zhang, X. *Ceram. Int.*
    2018, *44,* 19390–19396. doi:10.1016/j.ceramint.2018.07.170
39. Dong, S.; Ding, X.; Guo, T.; Yue, X.; Han, X.; Sun, J. *Chem. Eng. J.*
    2017, *316,* 778–789. doi:10.1016/j.cej.2017.02.017
40. Song, X.-Z.; Qiao, L.; Sun, K.-M.; Tan, Z.; Ma, W.; Kang, X.-L.;
    Sun, F.-F.; Huang, T.; Wang, X.-F. *Sens. Actuators, B* **2018,** *256,*
    374–382. doi:10.1016/j.snb.2017.10.081
41. Zhang, R.; Shi, J.; Zhou, T.; Tu, J.; Zhang, T. *J. Colloid Interface Sci.*
    2019, *539,* 490–496. doi:10.1016/j.jcis.2018.12.096
42. Zhou, X.; Li, X.; Sun, H.; Sun, P.; Liang, X.; Liu, F.; Hu, X.; Lu, G.
    ACS Appl. Mater. Interfaces **2015,** *7,* 15414–15421.
    doi:10.1021/acsami.5b03537
43. Zhang, R.; Zhang, T.; Zhou, T.; Lou, Z.; Deng, J.; Wang, L. *RSC Adv.*
    2016, *6,* 66738–66744. doi:10.1039/c6ra12201a
44. Kaur, J.; Anand, K.; Kaur, A.; Singh, R. C. *Sens. Actuators, B* **2018,**
    258, 1022–1035. doi:10.1016/j.snb.2017.11.159
45. Patil, J. Y.; Nadargi, D. Y.; Gurav, J. L.; Mulla, I. S.; Suryavanshi, S. S.
    Ceram. Int. **2014,** *40,* 10607–10613.
    doi:10.1016/j.ceramint.2014.03.041
46. Peng, S.; Wang, Z.; Liu, R.; Bi, J.; Wu, J. *Sens. Actuators, B* **2019,**
    288, 649–655. doi:10.1016/j.snb.2019.03.056
47. Liu, C.; Wang, B.; Wang, T.; Liu, J.; Sun, P.; Chuai, X.; Lu, G.
    Sens. Actuators, B **2017,** *248,* 902–909. doi:10.1016/j.snb.2017.01.133
48. Wang, Y.; Liu, F.; Yang, Q.; Gao, Y.; Sun, P.; Zhang, T.; Lu, G.
    Mater. Lett. **2016,** *183,* 378–381. doi:10.1016/j.matlet.2016.07.099
49. Qin, M.; Shuai, Q.; Wu, G.; Zheng, B.; Wang, Z.; Wu, H.
    Mater. Sci. Eng., B **2017,** *224,* 125–138.
    doi:10.1016/j.mseb.2017.07.016
50. Walker, J. M.; Akbar, S. A.; Morris, P. A. *Sens. Actuators, B* **2019,** *286,*
    624–640. doi:10.1016/j.snb.2019.01.049
51. Ni, Y.; Xu, J.; Liu, H.; Shao, S. *Talanta* **2018,** *185,* 335–343.
    doi:10.1016/j.talanta.2018.03.097
52. Abideen, Z. U.; Katoch, A.; Kim, J.-H.; Kwon, Y. J.; Kim, H. W.;
    Kim, S. S. *Sens. Actuators, B* **2015,** *221,* 1499–1507.
    doi:10.1016/j.snb.2015.07.120
53. Iftekhar Uddin, A. S. M.; Phan, D.-T.; Chung, G.-S. *Sens. Actuators, B*
    2015, *207,* 362–369. doi:10.1016/j.snb.2014.10.091